Simulation of blood flow past distal arteriovenous anastomosis with intimal hyperplasia

Luoding Zhu (祝罗丁) and Kaoru Sakai
Department of Mathematical Sciences,
Indiana University - Purdue University Indianapolis,
402 N Blackford Street, Indianapolis, IN 46202, USA.
Corresponding author: L Zhu, luozhu@iupui.edu

Late-stage-kidney-disease patients have to rely on hemodialysis for the maintenance of their regular lives. Arteriovenous graft (AVG) is one of the commonly used devices for dialysis. However, this artificially created shunt may get clotted and eventually causes the dialysis to fail. The culprit behind the AVG clotting and failure is the intimal hyperplasia (IH), the gradual thickening of vein-wall in the vicinity of the blood vessel-graft conjunctions. The mechanism of IH is not well understood despite extensive studies. In this work we investigate the effects of the IH development, including its location and severity on the flow and force fields in the distal AVG anastomosis using computational fluid dynamics (CFD). The stenosis due to IH is modelled in the shape of a Gaussian function with two free parameters. The blood is modelled as a viscous incompressible fluid, and the blood flow (pulsatile) is governed by the Navier-Stokes equations which are numerically solved by the lattice Boltzmann equations (D3Q19). The fluid-structure-interaction is modelled by the immersed boundary (IB) framework. Our computational results show that the IH severity has the most significant influences on the wall shear stress (WSS), wall normal stress (WNS), and the axial oscillating index (OSI). The stenosis location and flow pulsatility do not have pronounced effects on flow and force fields. Our results indicate that the IH progression tends to exacerbate the disease and accelerate the closure of the vein lumen, and hence the dialysis failure.

I. INTRODUCTION

Patients with end-stage renal disease (ESRD) need to rely on hemodialysis (HD) for maintaining their lives before kidney transplant. Dialysis needs vascular access for removing wastes in the blood. A major form of vascular access is by way of arteriovenous graft (AVG) made of polytetrafluoroethylene (PTFE). The AVG is surgically connected to an artery on one end and to a vein on the other end, generally in a patient's forearm and it stays there permanently. During dialysis two needles are inserted into the graft for taking blood from and returning blood to the patient.

One long-standing problem plaguing the dialysis practice since its invention is the initialization and development of intimal hyperplasia (IH), i.e, a gradual thickening of the innermost layer of the vessel wall in the vicinity of the two blood-vessel-graft anastomoses (distal and proximal). Progression of the disease can eventually lead to a full blockage of the vein lumen and failure of the AVG and dialysis[1,2]. (The alternative vascular access by arteriovenous fistula (AVF) faces similar issue [3]). Pathological studies found that the intimal hyperplasia (IH) is most severe around the vein-graft anastomosis.

In spite of extensive studies, the mechanism of intimal hyperplasia is not yet well understood. Currently it is commonly believed that the most important factors include the blood-vessel injuries and stimuli of blood-flow disturbances[4–7], both caused by AVG implantation. The native blood flow in the vein is slow and quasi-steady; the blood flow in the artery is fast and pulsatile. When the vein and artery are artificially connected by the AVG, the high speed pulsatile arterial flow rushes into the vein and causes significant disturbances in flows near the arteriovenous anastomosis. The flow disturbances alter the force fields, e.g., the the wall shear stress (WSS) and wall normal stress (WNS) on the innermost surface of 7 the vein wall, which is lined by a layer of vascular endothelial cells (VECs). These cells are found to be sensitive to the WSS, WNS, and their gradients[8–11]. The deviations of WSS and WNS from their normal biological ranges are perceived by the vascular endothelial cells (VECs), which intrigue a series of biochemical and biological signaling leading to excessive migration of vascular smooth muscle cells (VSMCs) into the innermost layer of the vein wall and out-of-control multiplication of the VSMCs in the layer, thus causing the thickening of the vein wall in the form of irregular protrusions into the lumen. Readers are referred to a recent review by Cunnane et al.[12] for contributing hemodynamic factors of intimal hyperplasia and a review by Loth et al.[13] on blood flow in end-to-side anastomoses.

There are already many studies on the flow and force fields near the blood-vessel-graft anastomoses *prior to* initialization and formation of the IH in literature. Grechy et al.[14] studied optimal design of a AVF configuration for reducing flow unsteadiness applying computational fluid dynamics. Fulker et al.[15] used CFD to study flow disturbance/turbulence caused by the needles during dialysis. Bai and Zhu [16–18] studied computationally the influences of various factors including elasticity of the graft and blood-vessel on the flow and force fields in the absence of IH.

However, to the best of our knowledge, there are no existing works studying the flow and force fields relevant to the 7 arteriovenous graft *in the presence of the IH*. As the progression of the intimal hyperplasia, the vein lumen gradually becomes narrower and more irregular, which may cause more and greater flow disturbances. And the flow and force fields in the vein may become even more deviated from the physiological ranges of the native vein flows prior to AVG implant. Hence, the IH progression may likely tend to exacerbate the

disease. Therefore, it is of significance to investigate the flow and force fields post IH formation.

It is challenging to model the development of the intimal hyperplasis because of many unknowns such as the geometry and location of the stenosis due to IH. See [19] for a one-dimensional model for the IH development. As a starting point, we build an ideal two-dimensional model for its shape, size, and location and combine it with a previously built vein-graft anastomosis model[16–18] to form a vein-graft-IH anastomosis model to be used in this work for simulation of blood flows past the venous AVG anastomosis in the presence of IH, focusing on the flow and force fields after the IH intialization. To the best of our knowledge, such studies do not exist in literature.

The remaining structure of the article is as follows. Section 2 details the model of the anastomosis with IH. Section 3 describes the mathematical formulation of the model problem. Section 4 briefs the numerical methods for the mathematical formulation. Section 5 reports major computational results. Section 6 concludes the paper with a summary.

II. MODEL PROBLEM

We use a rectilinear orthogonal coordinate system (Eulerian) for a model problem of blood flow through the distal AVG anastomosis with IH: x-axis points from the outlet to inlet of the vein along the vein's center line (horizontal), y-axis points from front to rear, and z-axis points from bottom to top on the vein-graft co-plane (vertical). See Fig. 1 (a).

It is challenging to model and simulate the initialization and development of the IH because the mechanism behind it is not clear yet. The geometry, size, position, and mechanical properties (e.g.Young's modulus) of the stenosis/thrombosis (protrusion of the vein wall into the lumen due to IH) may differ from patient to patient, and from location to location and time to time for a specific patient. Therefore it is virtually impossible to build a patient-specific physiologically realistic IH model. Budu-Grajdeanu, et. al. [19] introduced a time-dependent radial growth model for the IH. Sakthivel et al.[20] computationally investigated the effect of irregularity of axis-symmetric arterial stenosis on WSS. In this paper, as a first step towards to physiologically realistic IH model, we build an idealized IH *in-vitro* model as follows. We concentrate on a single IH protrusion (i.e. bulge or stenosis). The shape of the stenosis is approximated as the surface of the solid of revolution formed by a 360-degree-rotation of the graph of a Gaussian function of one argument about the vertical-axis (i.e. z-axis): $G(x) = \frac{1}{\sigma\sqrt{2\pi}} e^{\frac{-(x-\mu)^2}{2\sigma^2}}$. The IH severity is modelled by the parameter variance σ^2. The greater the σ^2, the severer the IH. Its location is modelled by the parameter mean μ, i.e., the center of peak. Three typical values are chosen for each of the two parameters to create three location models and three severity models: $\mu = 135, 167, 200$ in LB units (LB nodes used for all simulations reported here are $260 \times 60 \times 120$ along x,y, and z directions, respectively), corresponding to model L, M, R, respectively. The physical locations of the three models L,M,R are approximately at the 65%, 56%, and 46% of the vein length, measured from its inlet. The parameter $\sigma^2 = 23/30, 25/62, 30/103$ in LB units, corresponding to severity model A, B, and C, respectively. The models A,B,C correspond to a blockage of 25%, 50%, and 75%, respectively, of the lumen measured by the ratio of the thrombus height and vein diameter. A total of 9 stenosis IH models is available by different combinations of the three values of the two parameters. Since the mechanical properties of the IH stenosis such as as Young's modulus are not known in literature (the properties may vary with patient, location, and time as well) and the vein near the anastomosis tends to get stiffer as IH progresses, the vein-graft-IH model is assumed to be rigid in this study. Note that most of the computational works in literature related to flows in AVG use rigid models and it is known that rigid models tend to overestimate the WSS and WNS[16,17,21]. Notice that the vein-graft-thrombus is embedded/sustained in the the surrounding tissue which is modeled by springs plus viscous fluid. Similar approach is used in literature[22,23]. See Fig. 1 (a,b,c,d) for the three IH models (A,B,C) and three locations (L,M,R).We comment that intimal hyperplasia in dialysis also occurs on the graft near the anastomosis, which may involve other contributing factors such as material mismatch between vein and the graft (usually made from PTFE) and injury caused by implantation surgery. This case is not considered in the current work.

The IH stenosis/thrombus model is combined with (placed on top of) the vein-graft anastomosis model recently established by Bai and Zhu[16–18] to obtain the vein-graft-IH model (see Fig. 1 (a)) for computational studies of flow and force fields of blood flows past the vein-graft anastomosis after the IH formation. To be complete, a brief summary of the anastomosis model in[16–18] is given here. Two co-planar pipes (one being straight and the other being curved) of circular cross-section and different diameters are used to model the vein and graft at the initial time, respectively, using Peskin's immersed boundary framework[24]. Elastic springs immersed in viscous fluid are used to model the ambient tissue. The velocity profile in Fig. 1 (e) is imposed at the graft inlet and a fraction of its mean speed is imposed at the vein inlet. The original velocity profile is taken from[25] for modeling blood flow in human arm (brachial artery). Friction free is enforced at the vein outlet and we do not consider different kinds of vein downstream conditions. The blood is assumed to be a homogeneous, viscous, incompressible, Newtonian fluid and the blood flow is assumed to be laminar. Notice that blood is essentially non-Newtonian and the blood flow during the dialysis could be non-laminar. Because the vein/graft dimensions are relatively large for dialysis, the blood is reasonably assumed to be Newtonian. The blood flow is assumed to be laminar for simplicity. We refer readers interested in non-Newtonian aspect of blood flow to [26,27] and reference therein and turbulent aspect of blood flow to [28] and references therein.

There are many dimensionless parameters in the model problem. We point out that our current work focuses on investigation of possible effects of the presence and progression of the IH, including its shape, size, and location. Therefore many of these parameters are fixed: graft-vein diameter ra-

tio $R_{gv} = 0.67$, attaching angle $\theta = \pi/12$. We would like to point out that these values are realistic in the dialysis practice. Values used in literature are from 10^0 to 90^0 for vein-graft attaching angle and approximately from 0.5 to 1.0 for graft-vein diameter ratio (from 4*mm* to 10*mm* for diameter of the vein connecting to AVG)[29–37]. The flow Reynolds number $Re = 100$. The velocity used for Reynolds number is twice the mean of the pulsatile velocity profile on the graft inlet. The dimensionless velocity profile on the graft inlet V_v is taken from [16–18] (see Fig. 1 (e)). The original dimensional velocity waveform is taken from literature[25]. The velocity waveform was obtained using cardiac cycle model for blood flow in brachial artery which is often used for dialysis. Vein inlet speed equals to 0.244 of the mean value of the graft inlet velocity. See Fig. 1 for a diagram of the vein-graft-IH model used in this study.

III. MATHEMATICAL FORMULATION

The mathematical equations governing the motions of the vein, graft, and blood are described as follows.

$$\rho\left(\frac{\partial \mathbf{u}}{\partial t} + \mathbf{u}\cdot\nabla\mathbf{u}\right) = -\nabla p + \mu\Delta\mathbf{u} + \boldsymbol{f}_i(\boldsymbol{x},t), \tag{1}$$

$$\nabla\cdot\mathbf{u} = 0, \tag{2}$$

$$\boldsymbol{f}_i(\boldsymbol{x},t) = \int_\Gamma \boldsymbol{F}(\boldsymbol{\alpha},t)\delta(\boldsymbol{x} - \boldsymbol{X}(\boldsymbol{\alpha},t))d\boldsymbol{\alpha}, \tag{3}$$

$$\mathbf{F}(\boldsymbol{\alpha},t) = -\frac{1}{2}\frac{\partial}{\partial \mathbf{X}}\Big(\int_\Gamma \Big(K_s\Big(\Big|\frac{\partial \mathbf{X}(\boldsymbol{\alpha},\mathbf{t})}{\partial\boldsymbol{\alpha}}\Big| - 1\Big)^2 + K_b\Big|\frac{\partial^2\mathbf{X}(\boldsymbol{\alpha},t)}{\partial\boldsymbol{\alpha}^2}\Big|^2\Big)d\boldsymbol{\alpha}\Big), \tag{4}$$

$$\frac{\partial \mathbf{X}}{\partial t}(\boldsymbol{\alpha},t) = \mathbf{U}(\boldsymbol{\alpha},t), \tag{5}$$

$$\boldsymbol{U}(\boldsymbol{\alpha},t) = \int_\Omega \boldsymbol{u}(\boldsymbol{x},t)\delta(\boldsymbol{x} - \boldsymbol{X}(\boldsymbol{\alpha},t))\mathrm{d}\boldsymbol{x}. \tag{6}$$

Eqs. 1 and 2 govern the motions of the blood and structure (vein and graft), where $\mathbf{u}$, ρ, and p are fluid velocity, mass density, and pressure, respectively. The term $\boldsymbol{f}_i$ in Eq. 1 is the interaction force between the vein/graft and the blood, which is calculated from its Lagrangian equivalent $\boldsymbol{F}(\boldsymbol{\alpha},t)$ defined by Eq. 4, where $\boldsymbol{\alpha} = (\alpha_1,\alpha_2)$ and $\boldsymbol{X} = (x,y,z)$ denote two Lagrangian and three Eulerian coordinates of the two-dimensional surface $\mathbf{X}$ of the structure (vein-graft-IH), respectively. In Eq. 4, the integral computes the total elastic energy in the structure. The first term represents the contribution of stretching/compression and the second term represents contribution of bending. The letter δ denotes the classic Dirac delta function. The interaction force in Lagrangian form $\mathbf{F}$ is computed by the the principle of virtual work from elastic potential energy stored in the structure. The first derivative with respect to $\mathbf{X}$ is the variational derivative. The K_s and K_b are coefficients of compression/stretching and bending of the constitutive fibers of the structure. The velocity of the structure $\boldsymbol{U}(\boldsymbol{\alpha},t)$ is interpolated from the velocity of the fluid by Eq. 6. This equation enforces the no-slip condition on the boundary separating the fluid and structure. We refer readers interested in the immersed boundary formulation for fluid-structure-interaction to the review article[24].

IV. NUMERICAL METHOD

The lattice Boltzmann equations (the D3Q19 model) [38–46] are used for the solutions of the Navier-Stokes equations 1 and 2. The interaction force term is discretized by the approach introduced by Guo et al.[47]. Finite difference methods are used for discretizations of the remaining equations as in the conventional IB framework[24]. For example, trapezoidal rule is used for the definite integrals in Eqs. 3, 4, and 6; central difference is used for the spatial derivatives in Eq. 4, and backward Euler is used for the temporal derivative in Eq. 5. The cosine-function version in the IB methods[24] is used for discretization of the Dirac delta function. In particular, the integral in Eq. 4 is performed from fiber to fiber for all constitutive fibers of the structure. Along a given fiber (i.e. fixed value of α_2)), α_1 represents the Lagrangian coordinate of a point on the fiber. (The Eulerian coordinate of the point is $\mathbf{X}$). Time-varying velocity magnitude read from the velocity profile in Fig. 1 (e) is specified at all fluid grid points on the graft inlet which is perpendicular to the x-axis in all simulations. Given values of all variables at time step n, the values of dependent variables at next time step n+1 are updated as follows:

1). The Lagrangian force $\mathbf{F}$ is computed from the position of the structure $\mathbf{X}$ via Eq. 4;

2). The Eulerian force $\mathbf{f}_i$ is computed from Lagrangian force $\mathbf{F}$ via Eq. 3;

3). LB method is used for solving the Navier-Stokes equations, advancing the fluid velocity and pressure one time-step forward;

4). The structure velocity $\mathbf{U}$ is updated from the fluid velocity $\mathbf{u}$ via Eq. 6;

5). The structure position is updated from its velocity via Eq. 5.

6) Go to 1) for next time step.

V. MAJOR COMPUTATIONAL RESULTS

The characteristic quantities for nondimensionalization are fluid mass density ρ_0, vein diameter D_0, and the period of flow pulsatility T_0. These quantities in LB units are chosen as in all

simulations: $\rho_0 = 1.0, D_0 = 10$, and $T_0 = 9300$. All simulations reported in the paper are run up to 11 heart beats and all data reported here are taken from the 10^{th} cycle. The range of averaged WSS on the vein in our simulations are between 118.1 Pa and 131.1 Pa. These values are consistent with the values in literature for similar vein-graft systems which were found from less than 1 Pa to hundreds of Pa[29,30,34,36,37,48–50]. We point out that the solution to pressure from Navier-Stokes equations is up to a constant, i.e., adding any constant to a solution the resultant is still a solution. Since WNS includes the pressure, therefore, the dimensional values of WNS may not have physiological meanings. It is the variation of WNS on the vein that makes more sense, which can be seen from the WNS distributions given in this section.

The major computational results will be presented in terms of quantities of interest for the force field such as WSS, WNS and flow field such as OSI and velocity contours. The OSI is defined as follows:

$$OSI = \frac{1}{2}(1 - \frac{|\int_0^T \tau_w dt|}{\int_0^T |\tau_w| dt}) \tag{7}$$

Here τ_w is the WSS. Note that OSI equals to 0 for unidirectional flows and 0.5 for periodic flows. Therefore, a greater value of OSI indicates a more oscillatory flow which is potentially more harmful to the endothelial cells underlining the innermost layer of vascular wall. In all figures of WSS and WNS reported in this section, two color bars are used for the purposes of better visualization on the vein. The left bar is for the vein and the other is for the graft.

The report on major results will be arranged as follows. First the results in the presence of the IH are compared with those in the absence of the IH. Then the effects of the flow pulsatility, IH location, and IH severity on the flow and force fields are addressed, respectively. To gauge possible influence of flow pulsatility, results at three time instants (labeled as P, V, and S on panel (e) in Fig. 1) corresponding to the peak, valley, and stationary part of the imposed velocity profile on the AVG inlet are compared and analyzed. To investigate the possible influences of the location and severity of the IH, three IH models (A,B,C) with various level of severity are built and positioned at three different locations (L,M,R), corresponding to being situated to the left, middle and right of the vein-graft conjunction, on the vascular wall relative to where the graft meets the vein. Since the AVG is made of non-living material (PTFE), the focus of analysis is placed on the vascular wall.

1. IH versus non-IH

The normal cross-section of the inner-most blood vessel wall is circular. Development of the IH on the vascular wall renders an irregular cross-section. Due to the complexity of the actual physiological geometry of the IH bulge which is patient and time dependent, the IH shape is idealized and simplified as convolution of the graph of a Gaussian function $z(x) = \frac{1}{\sigma\sqrt{2\pi}} e^{\frac{-(x-\mu)^2}{2\sigma^2}}$ about z-axis for 2π with various mean μ and standard deviation σ.

A series of simulations with different combinations of IH models (severity and location) are conducted. In contrast, simulations with exactly the same parameters of the problem (the fluid, flow, AVG, and vein) but in the absence of the IH are also conducted. Results (distribution of WSS, WNS, and OSI on the vascular and AVG walls) at three time instants (P, V, S) are visualized and compared between the two scenarios. Fig. 2 gives some typical results (models A, M, R and instant P). In the figure, the first row is the OSI axial (i.e., OSI for flow along the axial direction), the second row is the OSI circumferential (i.e., OSI for flow along the circumferential direction), the third row is the WSS, and the last row is the WNS. The first column shows the non-IH case, the second and third columns show the case with IH located at the location M and R, respectively. From the figure, we can see that the presence of IH bulge (stenosis of lumen) has obvious influences on the distributions of the WSS, WNS, and OSI on the vascular wall. The OSI axial upstream of the anastomosis becomes quite different. Although the OSI downstream of the anastomosis looks remained almost the same (nearly unidirectional along axial direction) in this figure (model A), it does show oscillatory flow behavior behind the IH bump when its severity increases (e.g., see the OSI in the next figure).

The native blood flow in the vein is quasi-steady. When the AVG is introduced, the upstream of the anastomosis becomes unsteady and oscillatory due to the resistance of the pulsatile flow from the AVG (which induces secondary flows upstream). Interestingly, the axial flow downstream remains roughly unidirectional away from the IH thrombus (locally oscillatory immediately downstream of the thrombus). This may be maintained through the auto-adjustment of flow from the vein in response to the pulsatile flow from the AVG. (Note that vein is movable in the surrounding medium). After the IH development on the vascular wall, the original unidirectional vein flow encounters more resistance (from the flow of AVG and irregularly narrowed lumen) and the secondary flows upstream are altered and OSI becomes different.

Although not shown here, our results demonstrate that the differences seen in Fig. 2 becomes stronger and more apparent as the IH severity increases.

2. Flow pulsatility

Arterial blood flows are in nature pulsatile due to periodic heart beats. When the pulsatile arterial flows enter the vein through the AVG, the steady flow in the vein may become pulsatile as well. It is natural to ask how would the arterial flow pulsatility affect the flow and force fields in the vein. Interestingly, comparisons of WSS, WNS, and OSI (both circumferential and longitudial) on the vein wall at the three typical time instants do not show significant influences of the flow pulsatility on the distributions of these variables on the vein wall. And it remains so regardless of the IH location and severity. See Fig. 3 for a typical demonstration. (Therefore in the subsequent part of this section, only results at the instant P (peak) will be used for discussion.) This result here

is consistent with the previous findings[16–18] prior to IH formation. As a side point, Our result here may also explain why arterial blood flows being naturally pulsatile will not endanger human blood vessel system (although the underlying constitutive cells do not like flow disturbances).

3. IH location

Comparisons of results with different stenosis locations (models L, M, R) suggest that the influences of the IH location on the distributions of OSI (circumferential), WSS, and WNS on the vein wall are insignificant (model C) or indiscernible (models A and B). However, obvious differences in the OSI (axial) is seen among the three locations. In particular, the OSI (axial) in regions downstream of the stenosis is mostly zero (except where immediately behind the stenosis) indicating unidirectional flows. The OSI (axial) in the majority of the regions upstream of the stenosis is above zero indicating oscillatory flows present in front of the IH protrusion/bulge. This is caused by the interplay between the pulsatility of flows in AVG and resistance of the IH protrusion to the mainstream flows from the vein inlet. Our result indicates that the IH location does not have important influence on the flow and force fields, which suggests that it may not be significant to investigate or predict the whereabouts of the IH thrombi/protrusion in practise. This outcome seems to contradict the common sense of fluid dynamics: the location of an obstacle in a flow should affect the flow and force fields near the obstacle. However, in our case, the vein is movable, the flow is pulsatile, and Reynolds number is low. The interplay among these factors appear to have diminished the importance of IH location. Fig. 4 displays some typical results for model C (the most severe case).

4. IH severity

Comparisons with different IH severity (models A,B,C) show significant differences in the distributions of OSI, WSS and WNS on the vein wall, regardless of the IH locations. And the more severe the IH stenosis is, the more evident the differences are. Fig. 5 plots some typical results of the distributions of the OSI (the first two rows), WSS (the second row), and WNS (the third row) on the structure walls for the three IH severity models A (the first column), B (the second column), and C (the third column) at location R. From these figures, one can see that as the IH severity increases, the OSI (axial) remains roughly the same downstream of the IH location and becomes greater in some regions upstream of the IH location. The OSI (circumferential) becomes less in some regions both downstream and upstream. These indicate that the axial flow in the vein becomes more oscillatory in the upstream and the secondary flow becomes less oscillatory in the vein as the IH severity increases. The influences on the WSS and WNS are localized to the IH protrusion regions. Less portion of the region experiences high WSS but more portion of the region experiences greater WSS and WNS as the IH severity increases. Our results indicate that the IH severity is the most important factor that alters the flow and force fields in contrast to IH location and flow pulsatility.

The native blood flow in the vein prior to AVG implant is slow and steady; introduction of the AVG induces significant disturbances in the flow (and hence in the forces as well). Since these disturbances are sensed by endothelial cells lining the innermost layer of the vein and eventually lead to the initialization of the IH, i.e., thickening of the vein wall and narrowing of the lumen. The progression of the IH results in the increase in the IH severity, which in turn, according to our results here, will cause more disturbances in flow and force which will tend to exacerbate the disease. Therefore, it appears that the IH progression is an unstable biological process which tends to accelerate itself due to the more abnormal flow and force fields induced by the increasing IH severity. Hence, it is best to prevent the initialization of the IH in the first place. Since the ratio of non-dialysis period to dialysis period is approximately 6, it is desirable to stop the blood flow from artery to vein during the non-dialysis period. (Note that the AVG is permanently placed in the patient's forearm.) A device designed by G. Akingba for this purpose has been proposed and its efficacy has been studied[50,51]. Our results here substantiate the necessity of such a device.

5. Averaged WSS and WNS

Now let us look at the averaged WSS and WNS on different segments of the vein. The vein is divided into three segments: the segment containing the vein-graft conjunction (II), the segment to its left (I), and the segment to its right (III). The WSS and WNS are averaged in space on each segment for all the cases involving different combinations of the three IH locations and three levels of severity. The differences in the averaged WSS and WNS between each of these cases and the corresponding non-IH case (the base case) are plotted in Fig. 6. This difference is expressed as a percentage. The upper panel is the averaged WSS, the lower panel is the averaged WNS. The left, middle and right panels correspond to the left, middle, and right segment of the vein, respectively. In each panel, the vertical axis is the percentage difference (relative to the base values) in the averaged WSS (upper panel) and WNS (lower panel). The charts are presented using pyramid shapes, with its base representing the base case (non-IH case) and its apex pointing upward indicating an increase in the mean values above the base values and pointing downward indicating a decrease in mean values below the base values. The other two axes are IH location and severity: the left, middle and right columns correspond to the three IH locations L, M, and R, respectively; and the front, middle, and rear rows correspond to the three IH severity models A, B, and C, respectively.

From the figures one can see that the WSS is significantly altered in the left segment; the WNS is significantly altered in the right segment; and both are substantially altered in the middle segment. The WSS becomes much smaller than its base values in many cases which is caused by increased flow disturbances induced by IH protrusion. The WNS becomes

lower in segment I and higher in segment III, which in caused by expedited/slowed flows in the corresponding regions due to the presence of IH stenosis in the vein lumen. However, the changes in the averaged WSS on the entire vein (i.e. averaged over the three segments) relative to the base case due to the IH severity and location are comparable (insignificant in both cases).

6. Flow visualization

Finally flow visualization via velocity contours is shown in Fig. 7 for some typical cases. The top, middle and bottom panels correspond to model A, B, and C. The left panel plots the velocity contours on several cross-sections normal to the x-axis. The right panel plots the velocity contours on the middle plane normal to y-axis. From the figure we can see that velocity contours on the planes perpendicular to x-axis look similar in the three cases. This suggests that the IH severity does not have much influences on the secondary flows (flows on the y-z plane). The velocity contours on the planes perpendicular to the y-axis look similar in the vein in front of the stenosis but quite different behind the stenosis: they become less dense, particularly in the middle regions, as IH severity increases indicating that the flows downstream of the stenosis become more rapid because of narrower lumen due to severer IH.

VI. SUMMARY AND CONCLUSION

In summary, many simulations are performed on blood flow past a distal AVG anastomosis with stenosis/thrombus due to IH focusing on the WSS, WNS, and OSI on the vein wall as the shape/size and location of the stenosis are varied. The main conclusions are: 1) The presence of IH stenosis as a consequence of IH has significant influences on the flow and force fields (OSI, WSS, and WNS) in the vein near the anastomosis in contrast to the case prior to IH initialization.

2) The size of the IH protrusion (gauge of the IH severity) has significant influences on the OSI, WSS, and WNS on the vein near the anastomosis.

3) The flow pulsatility and stenosis location do not have pronounced influences on the OSI, WSS, and WNS on the vein.

Our computational results suggest that the development of the intimal hyperplasia is unstable, i.e., once it is initialized, the stenosis/thrombus tends to grow persistently until the vein lumen is completely obstructed. This seems to indicate that the best approach to tackle the AVG failure for dialysis is to prevent the IH formation in the first place rather than apply various means to improve the shunt patency post IH initialization.

Acknowledgments

This work was supported by the National Science Foundation (NSF) of the USA (research grants DMS-1522554 and DMS-1951531).We thank the unknown referees for their comments and suggestions which have led to a better presentation of our work. All authors declare no conflict of interest related to this work.

Data availablility statement

The data that support the findings of this study are available from the corresponding author upon reasonable request.

[1]S. J. Schwab, "Vascular access for hemodialysis," Kidney international **55**, 2078–2090 (1999).
[2]E. C. Kovalik and S. J. Schwab, "Can venous stenosis be prevented?" in *Seminars in Dialysis*, Vol. 12 (Wiley Online Library, 1999) pp. 144–145.
[3]A. Brahmbhatt, A. Remuzzi, M. Franzoni, and S. Misra, "The molecular mechanisms of hemodialysis vascular access failure," Kidney international **89**, 303–316 (2016).
[4]S. Unnikrishnan, T. N. Huynh, B. Brott, Y. Ito, C. Cheng, A. Shih, M. Allon, and A. S. Anayiotos, "Turbulent flow evaluation of the venous needle during hemodialysis," Journal of biomechanical engineering **127**, 1141–1146 (2005).
[5]T. N. Huynh, B. K. Chacko, X. Teng, B. C. Brott, M. Allon, S. S. Kelpke, J. A. Thompson, R. P. Patel, and A. S. Anayiotos, "Effects of venous needle turbulence during ex vivo hemodialysis on endothelial morphology and nitric oxide formation," Journal of biomechanics **40**, 2158–2166 (2007).
[6]O. Kh. Jahrome, I. Hoefer, G. J. Houston, P. A. Stonebridge, P. J. Blankestijn, F. L. Moll, and G. J. De Borst, "Hemodynamic effects of spiral eptfe prosthesis compared with standard arteriovenous graft in a carotid to jugular vein porcine model," The journal of vascular access **12**, 224–230 (2011).
[7]M. R. De Vries and P. H. Quax, "inflammation in vein graft disease," Frontiers in Cardiovascular Medicine **5**, 3 (2018).
[8]R. S. Reneman, T. Arts, and A. P. Hoeks, "Wall shear stress–an important determinant of endothelial cell function and structure–in the arterial system in vivo," Journal of vascular research **43**, 251–269 (2006).
[9]O. Traub and B. C. Berk, "Laminar shear stress: mechanisms by which endothelial cells transduce an atheroprotective force," Arteriosclerosis, thrombosis, and vascular biology **18**, 677–685 (1998).
[10]P. F. Davies, A. Remuzzi, E. J. Gordon, C. F. Dewey, and M. A. Gimbrone, "Turbulent fluid shear stress induces vascular endothelial cell turnover in vitro," Proceedings of the National Academy of Sciences **83**, 2114–2117 (1986).
[11]M. J. Thubrikar, *Vascular mechanics and pathology* (Springer Science & Business Media, 2007).
[12]C. V. Cunnane, E. M. Cunnane, and M. T. Walsh, "A review of the hemodynamic factors believed to contribute to vascular access dysfunction," Cardiovascular engineering and technology **8**, 280–294 (2017).
[13]F. Loth, P. F. Fischer, and H. S. Bassiouny, "Blood flow in end-to-side anastomoses," Annu. Rev. Fluid Mech. **40**, 367–393 (2008).
[14]L. Grechy, F. Iori, R. Corbett, S. Shurey, W. Gedroyc, N. Duncan, C. Caro, and P. Vincent, "Suppressing unsteady flow in arterio-venous fistulae," Physics of Fluids **29**, 101901 (2017).
[15]D. Fulker, B. Ene-Iordache, and T. Barber, "High-resolution computational fluid dynamic simulation of haemodialysis cannulation in a patient-specific arteriovenous fistula," Journal of biomechanical engineering **140**, 031011 (2018).
[16]Z. Bai, "Modeling and simulation of blood flow past the distal anastomosis of arteriovenous graft for hemodialysis," PhD Dissertation, Department of Mathematical Sciences, Indiana University - Purdue University Indianapolis (August 2018).
[17]Z. Bai and L. Zhu, "Three-dimensional simulation of a viscous flow past a compliant model of arteriovenous-graft anastomosis," Computers & Fluids **181**, 403–415 (2019).
[18]Z. Bai and L. Zhu, "Simulation of blood flow past a distal arteriovenous-graft anastomosis at low reynolds numbers," Physics of Fluids **31**, 091902 (2019).
[19]P. Budu-Grajdeanu, R. C. Schugart, A. Friedman, C. Valentine, A. K. Agarwal, and B. H. Rovin, "A mathematical model of venous neointimal hyperplasia formation," Theoretical Biology and Medical Modelling **5**, 2 (2008).
[20]M. Sakthivel and K. Anupindi, "An off-lattice boltzmann method for blood flow simulation through a model irregular arterial stenosis: The effects of amplitude and frequency of the irregularity," Physics of Fluids **33**, 031912 (2021).
[21]I. Decorato, Z. Kharboutly, C. Legallais, and A.-V. Salsac, "Numerical study of the influence of wall compliance on the haemodynamics in a patient-specific arteriovenous fistula," Computer Methods in Biomechanics and Biomedical Engineering **14**, 121–123 (2011).
[22]Y. Wu and X.-C. Cai, "A parallel two-level method for simulating blood flows in branching arteries with the resistive boundary condition," Computers & Fluids **45**, 92–102 (2011).
[23]M. Bukač, S. Čanić, J. Tambača, and Y. Wang, "Fluid–structure interaction between pulsatile blood flow and a curved stented coronary artery on a beating heart: a four stent computational study," Computer Methods in Applied Mechanics and Engineering **350**, 679–700 (2019).
[24]C. S. Peskin, "The immersed boundary method," Acta numerica **11**, 479–517 (2002).
[25]W. Quanyu, L. Xiaojie, P. Lingjiao, T. Weige, and Q. Chunqi, "Simulation analysis of blood flow in arteries of the human arm," Biomedical Engineering: Applications, Basis and Communications **29**, 1750031 (2017).
[26]J. Chen, X.-Y. Lu, and W. Wang, "Non-newtonian effects of blood flow on hemodynamics in distal vascular graft anastomoses," Journal of Biomechanics **39**, 1983–1995 (2006).
[27]C. Saengow, A. J. Giacomin, and A. S. Dimitrov, "Normal stress differences of human blood in unidirectional large-amplitude oscillatory shear flow," Journal of Fluids Engineering **142** (2020).
[28]L. Antiga and D. A. Steinman, "Rethinking turbulence in blood," Biorheology **46**, 77–81 (2009).
[29]P. Longest and C. Kleinstreuer, "Computational haemodynamics analysis and comparison study of arterio-venous grafts," Journal of medical engineering & technology **24**, 102–110 (2000).
[30]F. Loth, P. F. Fischer, N. Arslan, C. D. Bertram, S. E. Lee, T. J. Royston, W. E. Shaalan, and H. S. Bassiouny, "Transitional flow at the venous anastomosis of an arteriovenous graft: potential activation of the erk1/2 mechanotransduction pathway," Journal of Biomechanical Engineering **125**, 49–61 (2003).
[31]H. Haruguchi and S. Teraoka, "Intimal hyperplasia and hemodynamic factors in arterial bypass and arteriovenous grafts: a review," Journal of Artificial Organs **6**, 227–235 (2003).
[32]S.-W. Lee, D. S. Smith, F. Loth, P. F. Fischer, and H. S. Bassiouny, "Importance of flow division on transition to turbulence within an arteriovenous graft," Journal of biomechanics **40**, 981–992 (2007).
[33]J. A. Akoh, "Prosthetic arteriovenous grafts for hemodialysis," The journal of vascular access **10**, 137–147 (2009).
[34]H.-H. Kim, Y. H. Choi, S.-H. Suh, J. S. Lee, Y. H. Jung, and Y. H. So, "Arteriovenous graft modeling and hemodynamic interpretation," Open Journal of Fluid Dynamics **2**, 324 (2012).
[35]M. Sarmast, H. Niroomand-Oscuii, F. Ghalichi, and E. Samiei, "Evaluation of the hemodynamics in straight 6-mm and tapered 6-to 8-mm grafts as upper arm hemodialysis vascular access," Medical & biological engineering & computing **52**, 797–811 (2014).
[36]S. Khruasingkeaw, Y. Khunatorn, K. Rerkasem, and T. Srisuwan, "Wall shear stress distribution in arteriovenous graft anastomosis using computational fluid dynamics," International Journal of Pharma Medicine and Biological Sciences **5**, 71 (2016).
[37]D. Williams, "Computational fluid dynamics analysis of arteriovenous graft configurations," Engineering and Applied Science Theses & Dissertations. **340.** Washington University in St. Louis (2018).
[38]Y. H. Qian, "Lattice gas and lattice kinetic theory applied to the navier-stokes equations," Doktorarbeit, Universite Pierre et Marie Curie, Paris (1990).
[39]S. Chen and G. D. Doolen, "Lattice boltzmann method for fluid flows," Annual review of fluid mechanics **30**, 329–364 (1998).
[40]L.-S. Luo, "Unified theory of lattice Boltzmann models for nonideal gases," Physical review letters **81**, 1618 (1998).
[41]L. Zhu, G. He, S. Wang, L. Miller, X. Zhang, Q. You, and S. Fang, "An immersed boundary method based on the lattice boltzmann approach in three dimensions, with application," Computers & Mathematics with Applications **61**, 3506–3518 (2011).
[42]D. A. Wolf-Gladrow, *Lattice-gas cellular automata and lattice Boltzmann models: An Introduction*, 1725 (Springer, 2000).
[43]Z. Guo and C. Shu, *Lattice Boltzmann method and its applications in engineering*, Vol. 3 (World Scientific, 2013).
[44]H. Huang, M. Sukop, and X. Lu, *Multiphase lattice Boltzmann methods: Theory and application* (John Wiley & Sons, 2015).
[45]T. Krüger, H. Kusumaatmaja, A. Kuzmin, O. Shardt, G. Silva, and E. M. Viggen, "The lattice boltzmann method," Springer International Publishing **10**, 978–3 (2017).
[46]S. Succi, *The Lattice Boltzmann Equation: For Complex States of Flowing Matter* (Oxford University Press, 2018).
[47]Z. Guo, C. Zheng, and B. Shi, "Discrete lattice effects on the forcing term

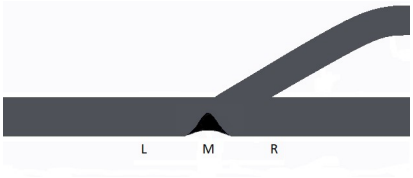

(a) AVG Model with stenosis in the model

(b) Stenosis model A

(c) Stenosis model B

(d) Stenosis model C

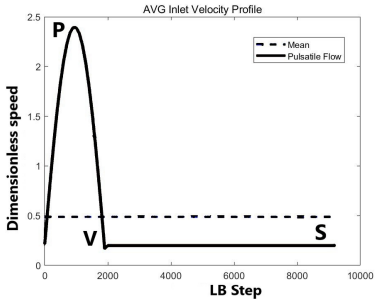

(e) AVG inlet speed profile

FIG. 1: Model Problem and AVG inlet velocity profile. (a) Vein-graft-IH model with three locations L, M, R. (b-d) Three stenosis models A,B,C. (e) AVG inlet velocity profile. In Fig. 1 (b), (c), (d) show the three IH severity models A, B, C. The black color represents the vein surface. The bottom curved part shows the IH shape and height. Each of these models is placed at the locations with labels L, M, R shown in Fig. 1(a) to form 9 IH models used in the paper.

in the lattice boltzmann method," Physical Review E **65**, 046308 (2002).

[48] J. M. Ortega, W. Small, T. S. Wilson, W. J. Benett, J. M. Loge, and D. J. Maitland, "A shape memory polymer dialysis needle adapter for the reduction of hemodynamic stress within arteriovenous grafts," IEEE Transactions on Biomedical Engineering **54**, 1722–1724 (2007).

[49] S. Misra, A. A. Fu, A. Puggioni, K. M. Karimi, J. N. Mandrekar, J. F. Glockner, L. A. Juncos, B. Anwer, A. M. McGuire, and D. Mukhopadhyay, "Increased shear stress with upregulation of vegf-a and its receptors and mmp-2, mmp-9, and timp-1 in venous stenosis of hemodialysis grafts," American Journal of Physiology-Heart and Circulatory Physiology **294**, H2219–H2230 (2008).

[50] A. McNally, A. G. Akingba, and P. Sucosky, "Effect of arteriovenous graft flow rate on vascular access hemodynamics in a novel modular anastomotic valve device," The Journal of Vascular Access **19**, 446–454 (2018).

[51] A. McNally, A. G. Akingba, E. A. Robinson, and P. Sucosky, "Novel modular anastomotic valve device for hemodialysis vascular access: preliminary computational hemodynamic assessment," The journal of vascular access **15**, 448–460 (2014).

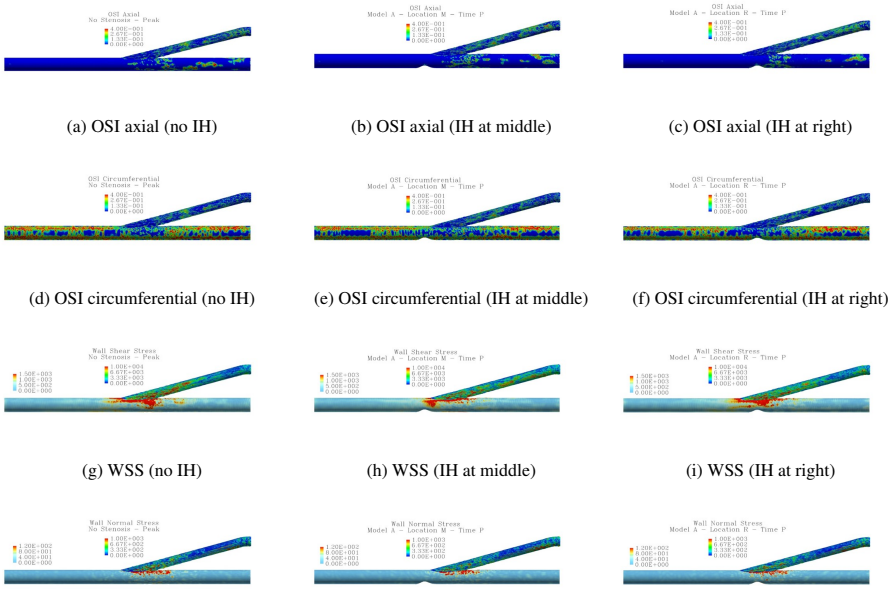

(a) OSI axial (no IH) (b) OSI axial (IH at middle) (c) OSI axial (IH at right)

(d) OSI circumferential (no IH) (e) OSI circumferential (IH at middle) (f) OSI circumferential (IH at right)

(g) WSS (no IH) (h) WSS (IH at middle) (i) WSS (IH at right)

(j) WNS (no IH) (k) WNS (IH at middle) (l) WNS (IH at right)

FIG. 2: Comparison of cases with and without IH. (a) OSI axial for no-IH case. (b) OSI axial with IH model A and location M. (c) OSI axial with IH model A and location R. (d) OSI circumferential for no-IH case. (e) OSI circumferential with IH model A and location M. (f) OSI circumferential with IH model A and location R. (g) WSS for no-IH case. (h) WSS with IH model A and location M. (i) WSS with IH mode A and location R. (j) WNS for no-IH case. (k) WNS with IH model A and location M. (l) WNS with IH mode A and location R.

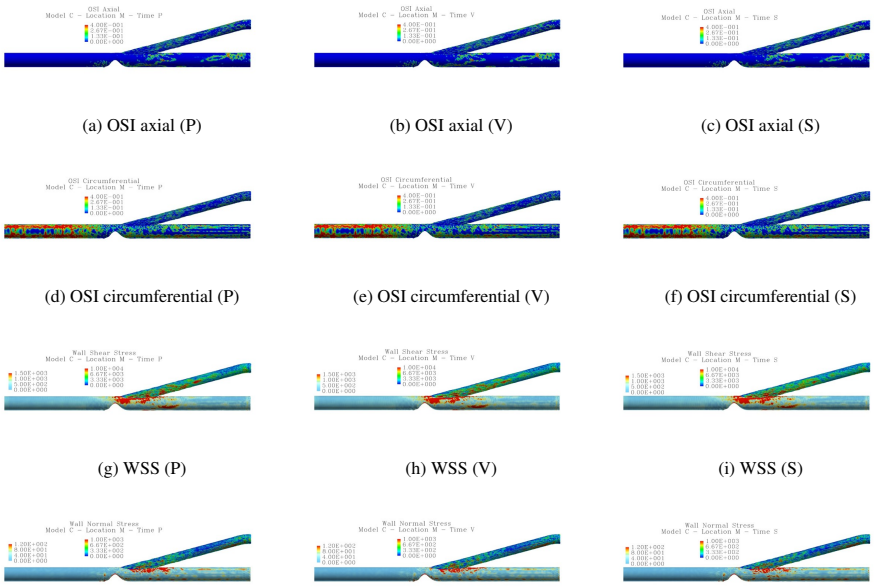

(a) OSI axial (P) (b) OSI axial (V) (c) OSI axial (S)

(d) OSI circumferential (P) (e) OSI circumferential (V) (f) OSI circumferential (S)

(g) WSS (P) (h) WSS (V) (i) WSS (S)

(j) WNS (P) (k) WNS (V) (l) WNS (S)

FIG. 3: Influence of flow pulsatility. (a) OSI axial for model C on location M at instant P. (b) OSI axial for model C on location M at instant V. (c) OSI axial for model C on location M at instant S. (d) OSI circumferential for model C on location M at instant P. (e) OSI circumferential for model C on location M at instant V. (f) OSI circumferential for model C on location M at instant S. (g) WSS for model C on location M at instant P. (h) WSS for model C on location M at instant V. (i) WSS for model C on location M at instant S. (j) WNS for model C on location M at instant P. (k) WNS for model C on location M at instant V. (l) WNS for model C on location M at instant S.

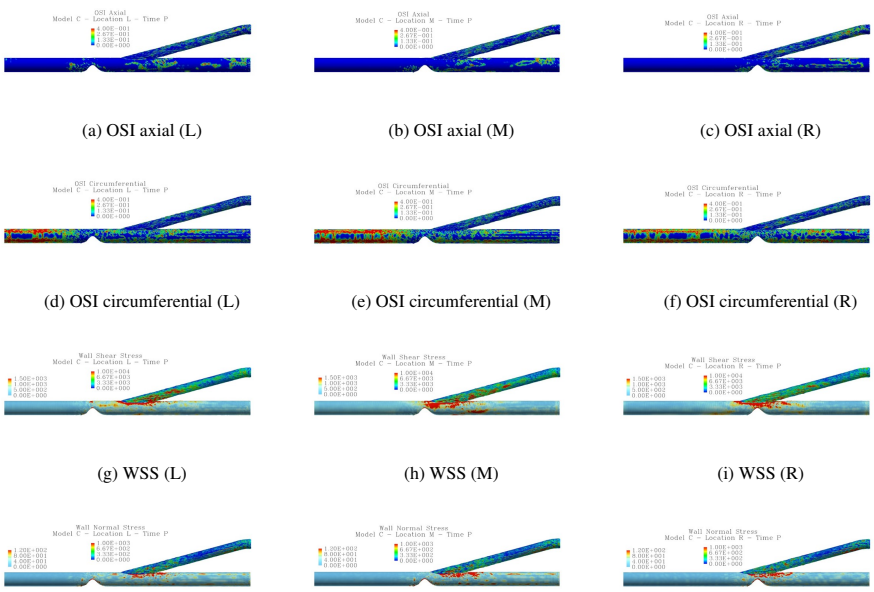

(a) OSI axial (L) (b) OSI axial (M) (c) OSI axial (R)

(d) OSI circumferential (L) (e) OSI circumferential (M) (f) OSI circumferential (R)

(g) WSS (L) (h) WSS (M) (i) WSS (R)

(j) WNS (L) (k) WNS (M) (l) WNS (R)

FIG. 4: Influence of stenosis location model. (a) OSI axial for model C on location L. (b) OSI axial for model C on location M. (c) OSI axial for model C on location R. (d) OSI circumferential for model C on location L. (e) OSI circumferential for model C on location M. (f) OSI circumferential for model C on location R. (g) WSS for model C on location L. (h) WSS for model C on location M. (i) WSS for model C on location R. (j) WNS for model C on location L. (k) WNS for model C on location M. (l) WNS for model C on location R.

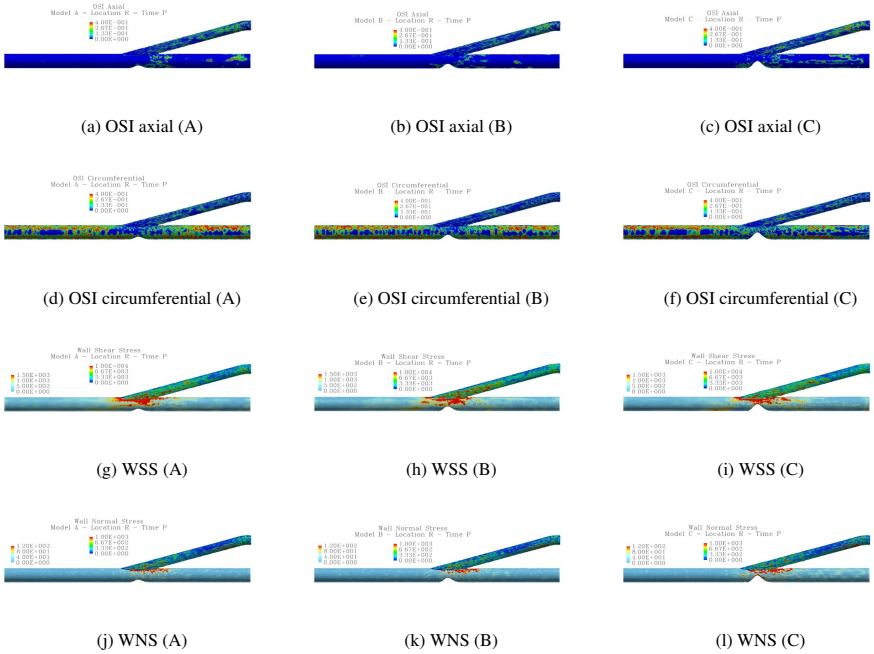

(a) OSI axial (A) (b) OSI axial (B) (c) OSI axial (C)

(d) OSI circumferential (A) (e) OSI circumferential (B) (f) OSI circumferential (C)

(g) WSS (A) (h) WSS (B) (i) WSS (C)

(j) WNS (A) (k) WNS (B) (l) WNS (C)

FIG. 5: Influence of stenosis severity. (a) OSI axial for model A on location R. (b) OSI axial for model B on location R. (c) OSI axial for model C on location R. (d) OSI circumferential for model A on location R. (e) OSI circumferential for model B on location R. (f) OSI circumferential for model C on location R. (g) WSS for model A on location R. (h) WSS for model B on location R. (i) WSS for model C on location R. (j) WNS for model A on location R. (k) WNS for model B on location R. (l) WNS for model C on location R.

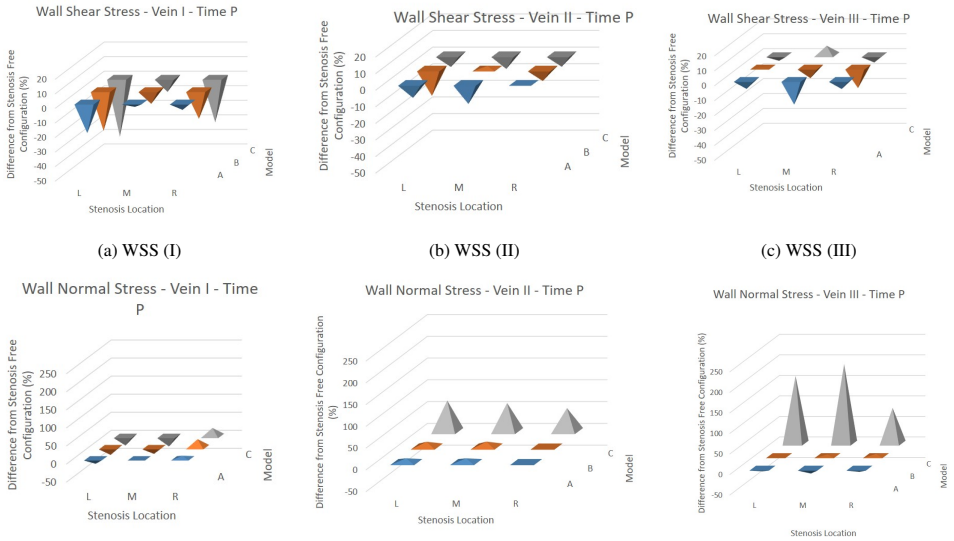

(a) WSS (I) (b) WSS (II) (c) WSS (III)

(d) WNS (I) (e) WNS (II) (f) WNS (III)

FIG. 6: Averaged WSS and WNS on three segments of the vein. (a) WSS on segment I. (b) WSS on segment II. (c) WSS on segment III. (d) WNS on segment I. (e) WNS on segment II. (f) WNS on segment III.

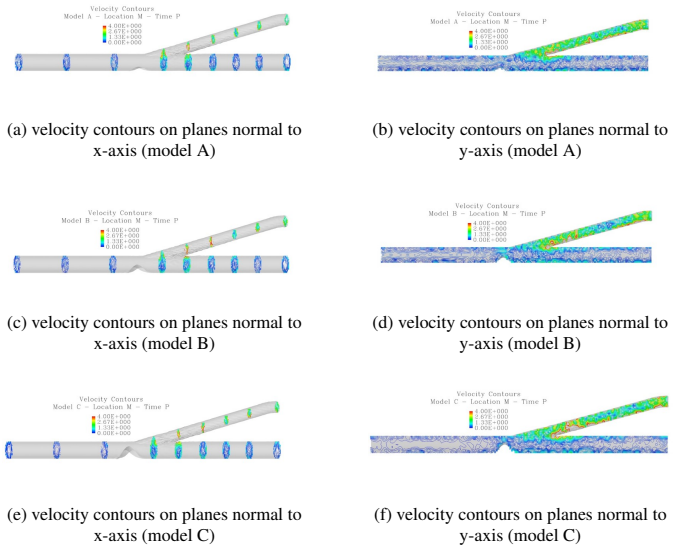

(a) velocity contours on planes normal to x-axis (model A)

(b) velocity contours on planes normal to y-axis (model A)

(c) velocity contours on planes normal to x-axis (model B)

(d) velocity contours on planes normal to y-axis (model B)

(e) velocity contours on planes normal to x-axis (model C)

(f) velocity contours on planes normal to y-axis (model C)

FIG. 7: Flow visualization. (a) velocity contours on planes normal to x-axis for model A. (b) velocity contours on planes normal to y-axis for model A. (c) velocity contours on planes normal to x-axis for model B. (d) velocity contours on planes normal to y-axis for model B. (e) velocity contours on planes normal to x-axis for model C. (f) velocity contours on planes normal to y-axis for model C.